Electronic Supplementary Information (ESI)

Substitution (CH_3, Cl, or Br) effects of the Imidazolate Linker on Benzene Adsorption kinetics for Zeolitic Imidazolate Framework (ZIF)-8

Ryohei Yagi [a], Takahiro Ueda*[a,b]

[a]*Department of Chemistry, Graduate School of Science, Osaka University, Toyonaka, Osaka 560-0043, Japan.*

[b]*The Museum of Osaka University, Osaka University, Toyonaka, Osaka 560-0043, Japan.*

Contents:

1. Figures for Supplementary Information

The lists of Figures;

- Figure S1. Thermogravimetry and differential thermal analysis diagrams.
- Figure S2. Nitrogen adsorption isotherms of X-ZIF-8.
- Figure S3. Powder X-ray diffraction (PXRD) patterns of X-ZIF-8.
- Figure S4. The SEM images of X-ZIF-8.
- Figure S5. Size distribution of the crystallites of X-ZIF-8.
- Figure S6. Comparison of the data optimization of a surface barrier model and an intra-crystalline (Fick) diffusion model.
- Figure S7. The typical example of the model structure for a 6-membered ring aperture in the case of ZIF-8
- Figure S8. The typical examples of the stable configuration of a benzene molecule adsorbed on a 6-membered ring aperture of X-ZIF-8.
- Figure S9. Arrhenius plot of the adsorption rate constant.
- Figure S10. Infrared spectra of X-ZIF-8.
- Figure S11. The results of the deconvolution of the ^{13}C-NMR resonance peaks.

2. Tables for Supplementary Information

Lists of Tables;

- Table S1. BET surface area and pore volume for ZIF-8 and X-ZIF-8.
- Table S2. Average particle size of ZIF-8 and X-ZIF-8.
- Table S3. Desorption amount of benzene from ZIF-8 and X-ZIF-8 after saturation of adsorption.
- Table S4. Results of the non-linear least-squares data fitting for Arrhenius plot of the adsorption rate constant.
- Table S5. Band assignment of IR spectrum of ZIF-8 before and after benzene adsorption.
- Table S6. Band assignment of IR spectrum of Cl-ZIF-8 before and after benzene adsorption.

- Table S7. Band assignment of IR spectrum of Br-ZIF-8 before and after benzene adsorption.
- Table S8. Band assignment of IR spectrum of benzene in bulk liquid and in X-ZIF-8.
- Table S9. The parameters characterizing the ^{13}C NMR resonance lines in ZIF-8 and ZIF-8/C_6H_6.
- Table S10. The parameters characterizing the ^{13}C NMR resonance lines in Cl-ZIF-8 and Cl-ZIF-8/C_6H_6.
- Table S11. The parameters characterizing the ^{13}C NMR resonance lines in Br-ZIF-8 and Br-ZIF-8/C_6H_6.

3. Evaluation of activation entropy of benzene trapped by 6-membered ring aperture

4. ^{13}C-^{14}N and ^{13}C-$^{79/81}Br$ residual dipolar splitting

1. Figures for Supplementary Information

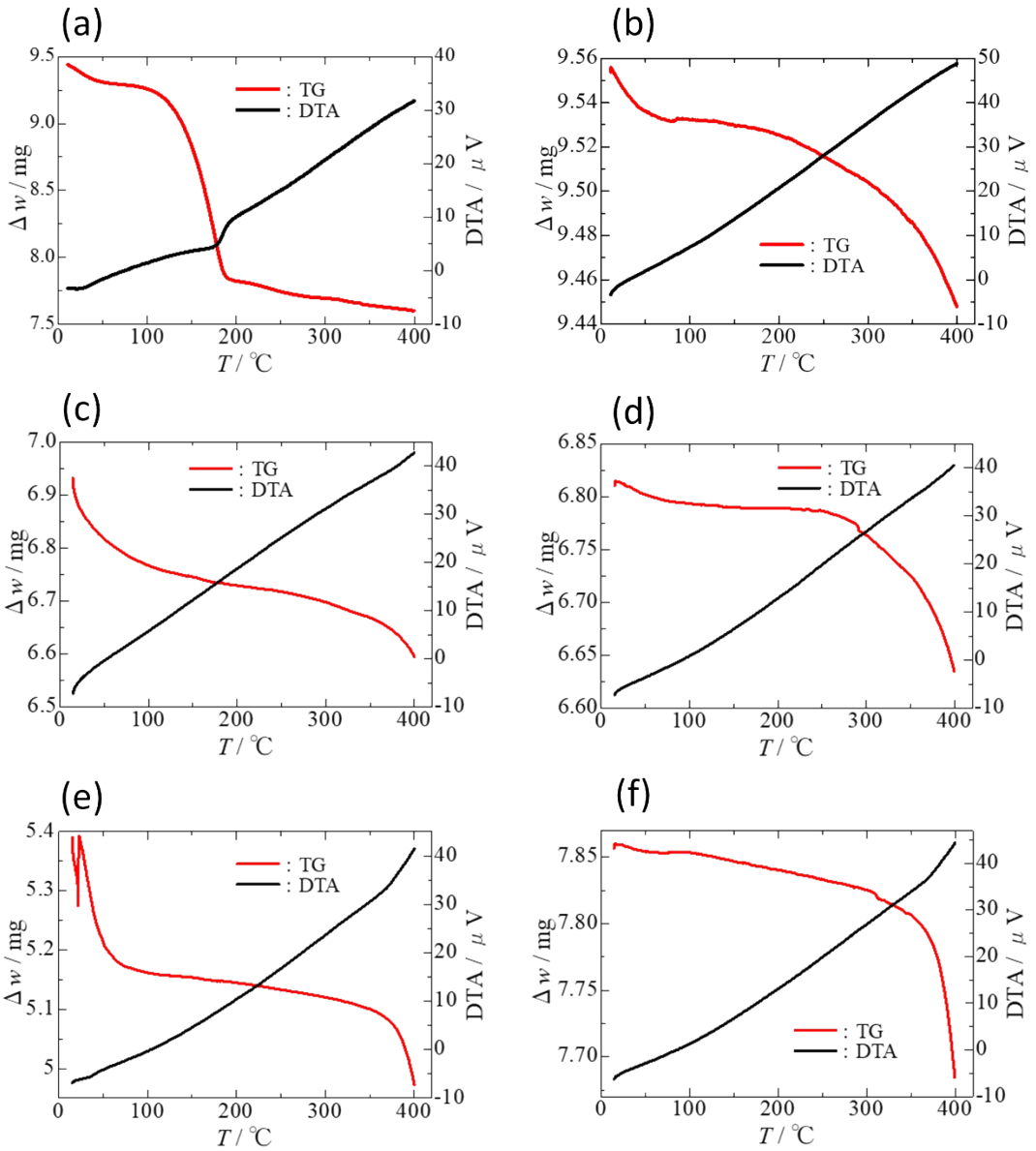

Figure S1. Thermogravimetry and differential thermal analysis diagrams; as-synthesized specimen of ZIF-8 (a), Cl-ZIF-8 (c) and Br-ZIF-8 (e), and pretreated specimen of ZIF-8 (b), Cl-ZIF-8 (d) and Br-ZIF-8 (f).

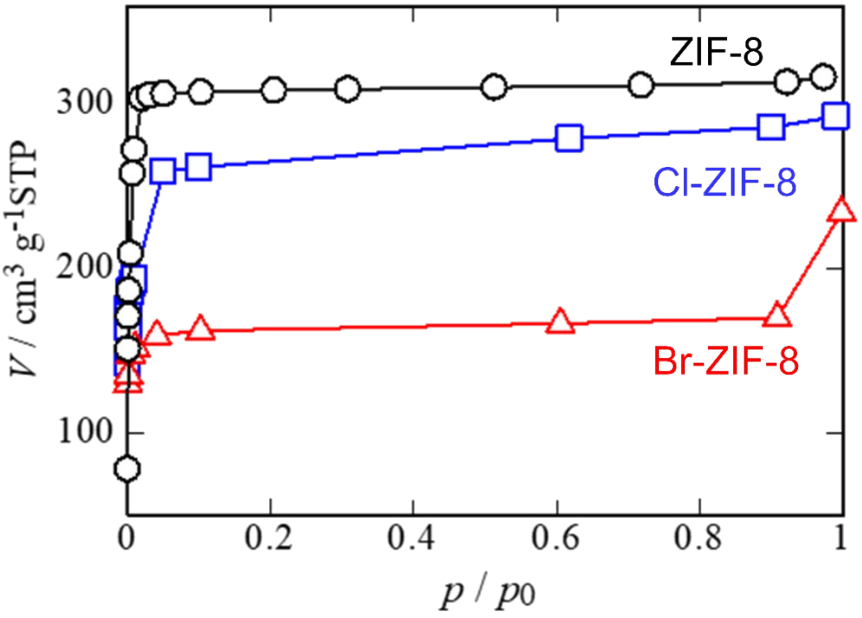

Figure S2. Nitrogen adsorption isotherms of ZIF-8 (ᔓ), Cl-ZIF-8 (●), and Br-ZIF-8 (❒).

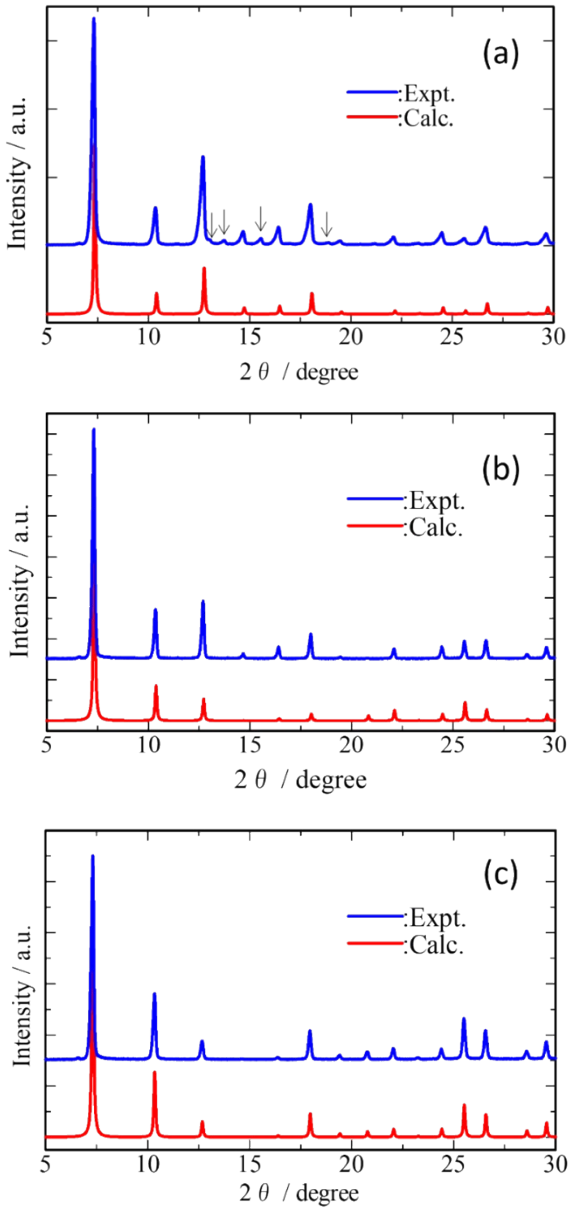

Figure S3. Powder X-ray diffraction (PXRD) patterns of ZIF-8 (a), Cl-ZIF-8 (b), and Br-ZIF-8 (c). The experimental powder patterns are in agreement with the calculated ones. In ZIF-8, the reflections denoted by arrows correspond to a trace amount of the by-product of $Zn_5(OH)_8(NO_3)_2$.

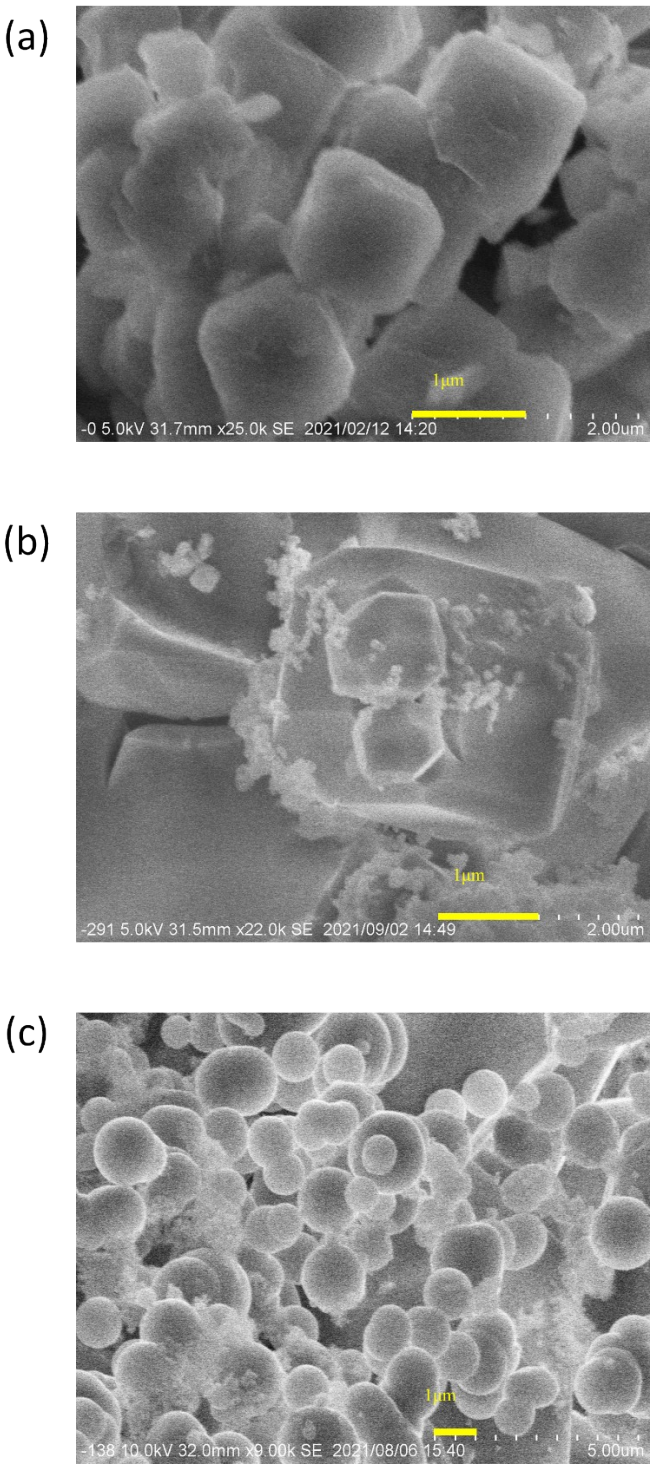

Figure S4. The SEM images of ZIF-8 (a), Cl-ZIF-8 (b), and Br-ZIF-8 (c).

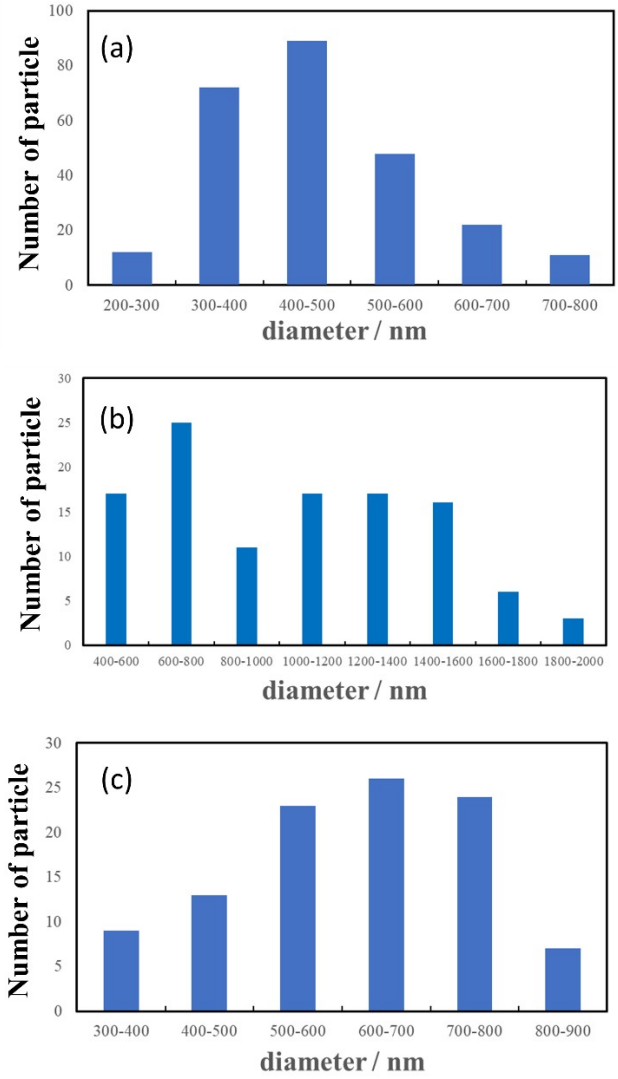

Figure S5. Size distribution of the crystallites determined from the SEM image; ZIF-8 (a), Cl-ZIF-8 (b), and Br-ZIF-8 (c). The average particle radii of r_{ave} are listed in Table S2.

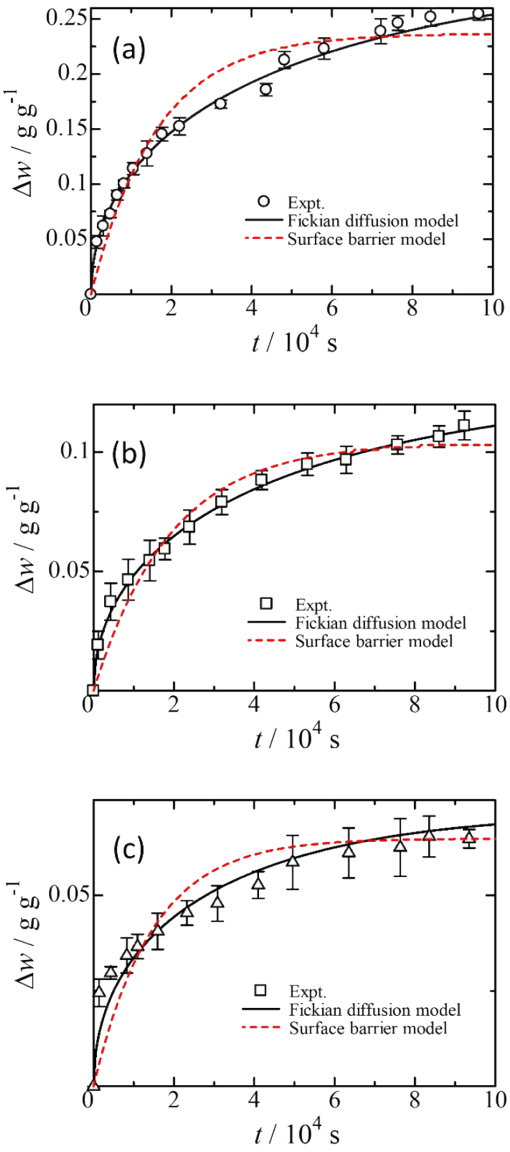

Figure S6. Comparison of the optimization of a surface barrier model and an intra-crystalline (Fick) diffusion model to the experimental data of the time dependence of the benzene uptake; ZIF-8 (a), Cl-ZIF-8 (b), and Br-ZIF-8 (c).

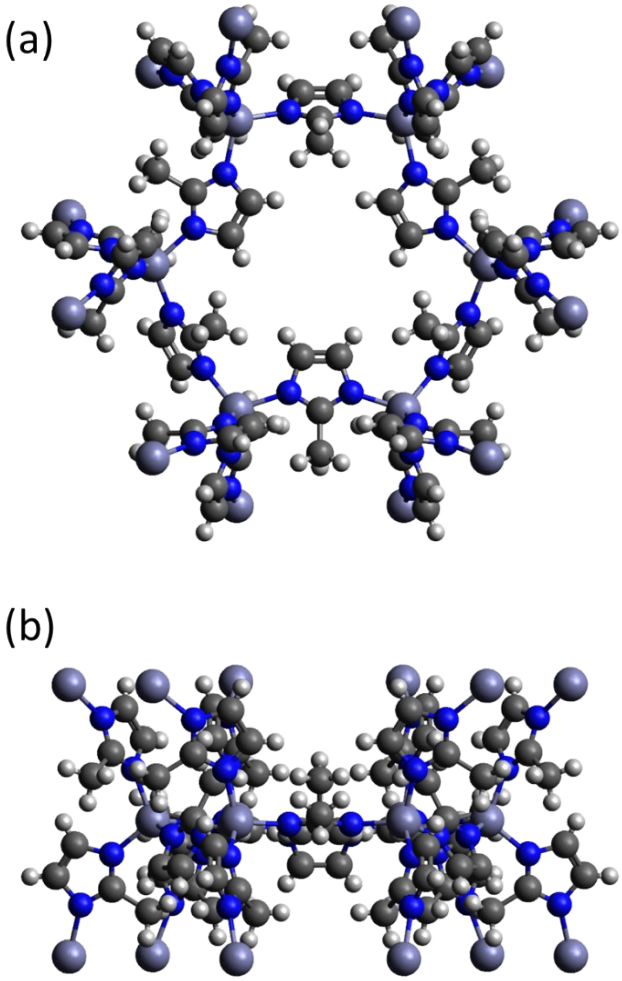

Figure S7. The typical example of the model structure for a 6-membered ring aperture in the case of ZIF-8; the vertical view of the aperture (a) and the horizontal view of the aperture (b). This structure of the 6-membered ring aperture is extracted from the crystal structure of ZIF-8. The zinc, carbon, nitrogen, and hydrogen atoms are colored by dark blue, gray, blue, and white, respectively.

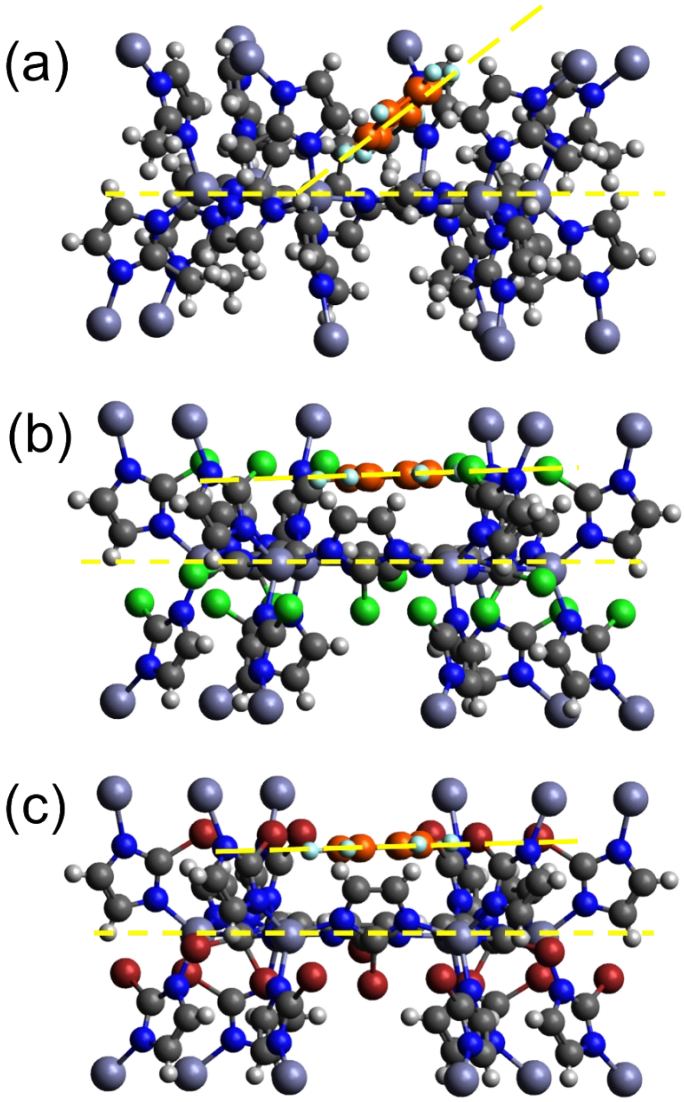

Figure S8. The typical example of the stable configuration of a benzene molecule adsorbed on a 6-membered ring aperture; ZIF-8 (a), Cl-ZIF-8 (b), and Br-ZIF-8 (c). These configurations were obtained by molecular mechanics calculation using Avogadro software. The carbon atoms and the hydrogen atoms in benzene molecules are displayed in orange and cyan balls, respectively. In the 6-membered ring aperture, the zinc, carbon, nitrogen, and hydrogen atoms are colored by dark blue, gray, blue, and white, respectively. The yellow dashed lines are guides to the eye to show the tilting angle between the benzene molecular plane and the aperture plane.

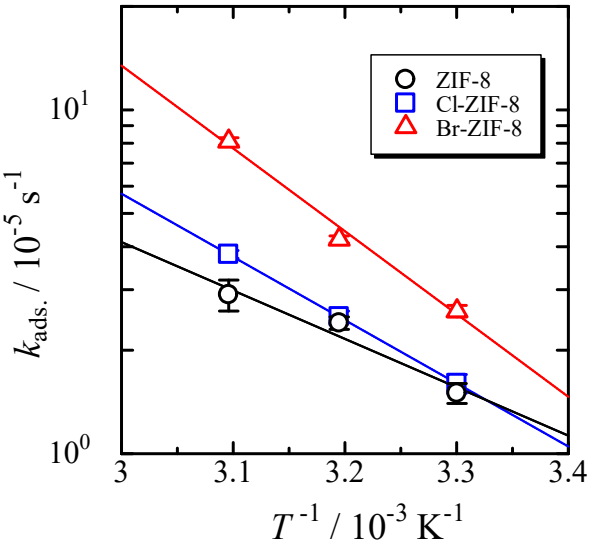

Figure S9. Arrhenius plot of the adsorption rate constant. The solid lines are the results of the optimization of Arrhenius law to the data using the least squares method. The parameters obtained are listed in Table S4.

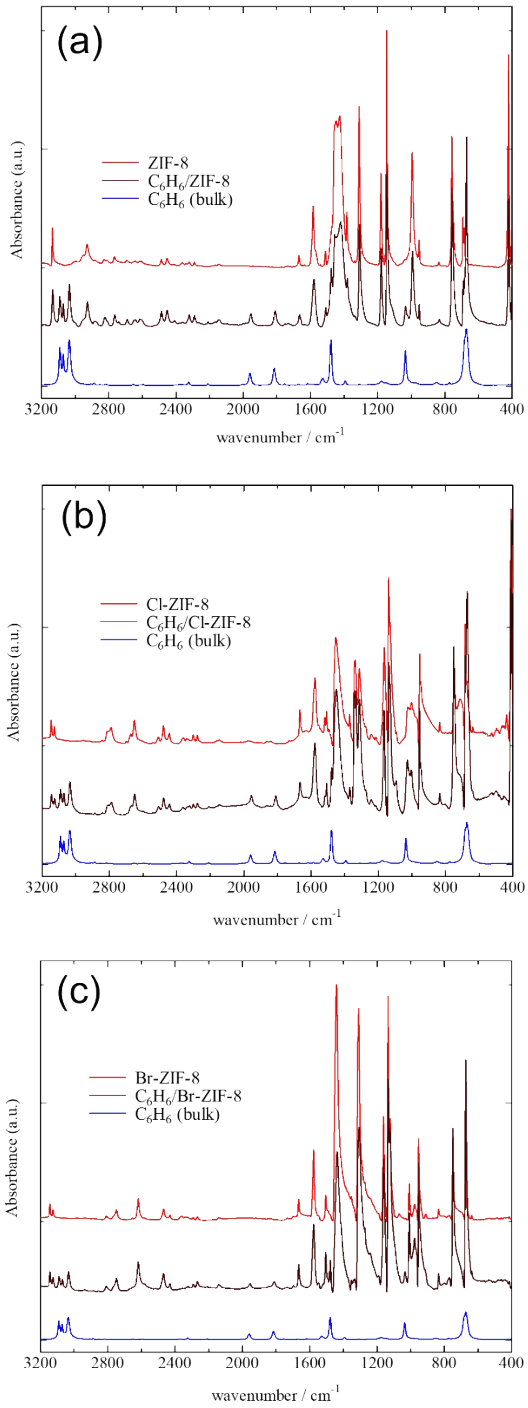

Figure S10. Infrared spectra of ZIF-8 (a), Cl-ZIF-8 (b), and Br-ZIF-8 (b) before and after benzene adsorption, in addition to the spectrum of bulk benzene, in the wavenumber range from 400 cm^{-1} to 3200 cm^{-1}.

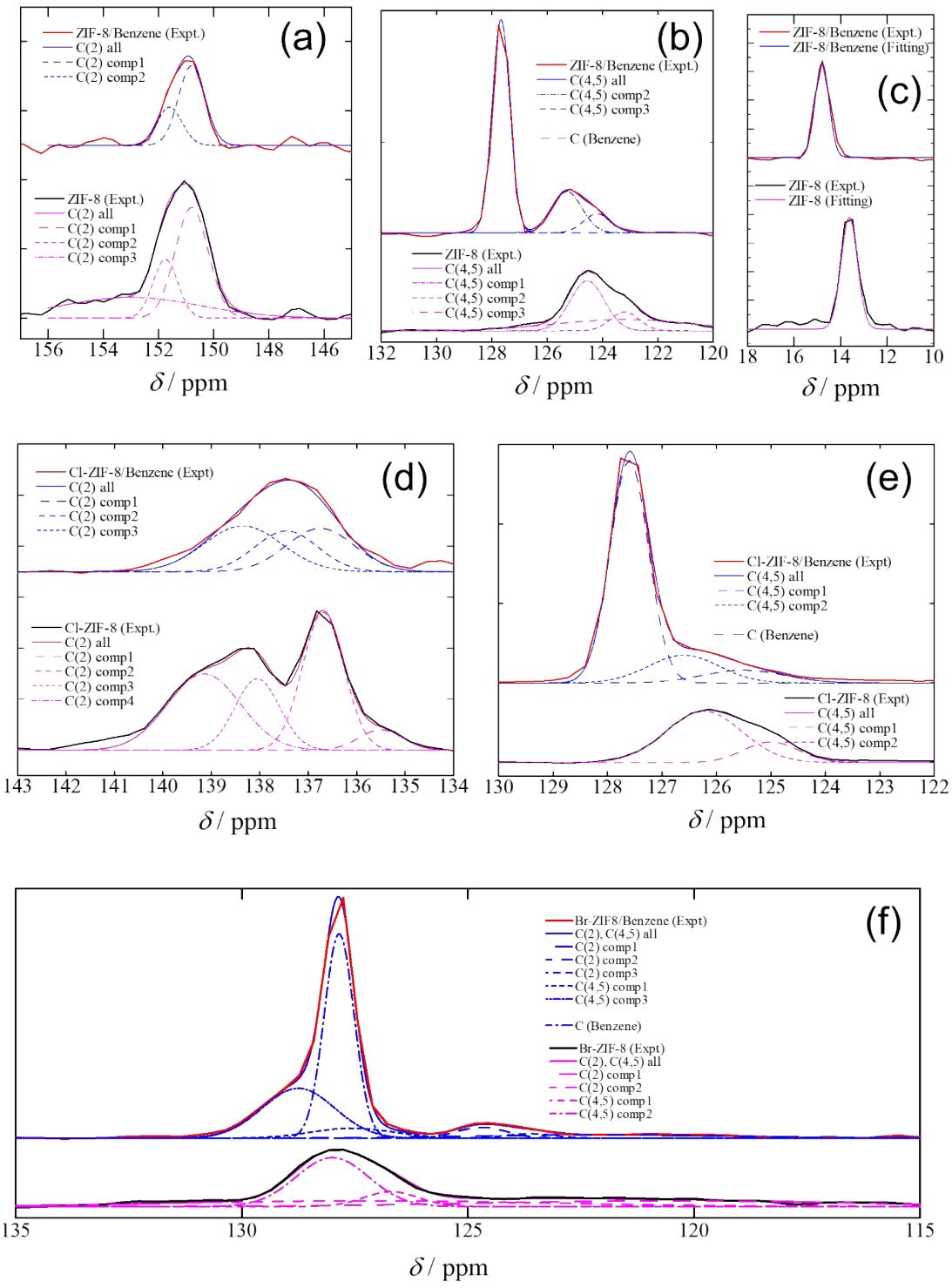

Figure S11. The results of the deconvolution of the resonance peaks using Gaussian functions: the quaternary carbon (a), the aromatic C-H carbons (b), and the methyl carbon (c) in ZIF-8, the quaternary carbon (d) and the aromatic C-H carbons (e) in Cl-ZIF-8, all carbons in Br-ZIF-8 (f).

2. Tables for Supplementary Information

Table S1. BET surface area and pore volume for ZIF-8 and X-ZIF-8.

	a_{BET} / m^2 g^{-1}	V_{pore} / cm^3 g^{-1}	V_{pore} / nm^3 (a pore)
ZIF-8	1310	0.49	1.1
Cl-ZIF-8	1052	0.45	1.2
Br-ZIF-8	660	0.26	0.93

Table S2. Average particle size of ZIF-8 and X-ZIF-8.

	d_{ave} / nm
ZIF-8	470 (± 100)
Cl-ZIF-8	1170 (± 200)
Br-ZIF-8	640 (± 100)

$r_{ave} = d_{ave}/2$

Table S3. Desorption amount of benzene from ZIF-8 and X-ZIF-8 after saturation of adsorption.

	$w_{initial}$/mg	$w_{desorption}$/mg	a_{sat}/g g^{-1}
ZIF-8	6.13	1.75	0.29
Cl-ZIF-8	8.04	1.12	0.14
Br-ZIF-8	8.01	0.66	0.082

Table S4. Results of the non-linear least-squares data fitting for Arrhenius plot of the adsorption rate constant.

	E_a/R / 10^3 K^{-1}	SE in E_a/R	$k_{0,ads}/10^{-5}$ s^{-1}	SE in $k_{0,ads}$	R^2
ZIF-8	3.2405848	± 0.019345149	6.8790369E+4	± 24.708053	0.939356
Cl-ZIF-8	4.232818	± 4.1879702E-6	1.8667184E+6	± 2.0093008E-4	1
Br-ZIF-8	5.5457234	± 0.014130175	2.2609365E+8	± 41.95949	0.989001

Table S5. Band assignment of IR spectrum of ZIF-8 before and after benzene adsorption.

	ZIF-8		ZIF-8	ZIF-8/C_6H_6
Band assignment [a]	$\tilde{\nu}_{Calc.}$[b]/cm^{-1}	$\tilde{\nu}_{Expt.}$[b]/cm^{-1}	$\tilde{\nu}_{Obs.}$/cm^{-1}	$\tilde{\nu}_{Obs.}$/cm^{-1}
Methyl in-plane bend (S)	414	422	421	421
Methyl stretch+ Ring puckering (S)	667	692	693	692
H_{ring} symmetric out-of-plane bend (S)	734	757	758	757
Ring in-plane bend (W/VW)	940	951	953	952
H_{methyl} bend (S)	981	995	995	994
H_{ring} scissor+H_{methyl} bend (VW)	1011	1038	1037	1034
H_{ring} wag (S)	1141	1145	1146	1145
Ring breathing (C-N symmetric stretch) (S)	1192	1175	1180	1179
H_{methyl} scissor(M)	1308	1307	1310	1309
Ring deformation (C-N asymmetric stretch) (S)	1369	1383	1382	1379
H_{methyl} bend (S)	1403	1420	1426	1424
C=C stretch+Cring-Cmethyl stretch (W)	1442	1512	1510	1509
Ring breathing (C=C stretch) (M)	2951	2927	1584	1579
H_{methyl} symmetric stretch (W)	3013	2927	2929	2926
H_{ring} symmetric stretch (M)	3180	3135	3134	3132

a) Ref. [S1]

b) Ref. [S2]

Table S6. Band assignment of IR spectrum of Cl-ZIF-8 before and after benzene adsorption.

	Cl-ZIF-8	Cl-ZIF-8/C_6H_6
Band assignment	$\tilde{\nu}_{Obs.}$/cm^{-1}	$\tilde{\nu}_{Obs.}$/cm^{-1}
Methyl in-plane bend (S)	410	410
Methyl stretch + Ring puckering (S)	683	682
H_{ring} symmetric out-of-plane bend (S)	749	750
H_{ring} scissor + H_{methyl} bend (VW)	1024	1026
H_{ring} wag (S)	1137	1136
Ring breathing (C-N symmetric stretch) (S)	1164	1165
H_{ring} wag (M)	1312	1312
Ring deformation (C-N asymmetric stretch) (S)	1371	1370
H_{methyl} bend (S)	1454	1449
C=C stretch+Cring-Cmethyl stretch (W)	1507	1507
H_{ring} symmetric stretch (M)	3127	3125
H_{ring} symmetric stretch (M)	3146	3144

Table S7. Band assignment of IR spectrum of Br-ZIF-8 before and after benzene adsorption.

	Br-ZIF-8	Br-ZIF-8/C_6H_6
Band assignment	$\tilde{\nu}_{Obs.}$/cm^{-1}	$\tilde{\nu}_{Obs.}$/cm^{-1}
Ring puckering (S)	675	672
H_{ring} symmetric out-of-plane bend (S)	749	748
H_{ring} symmetric out-of-plane bend (S)	834	834
H_{ring} symmetric out-of-plane bend (S)	952	951
H_{ring} symmetric out-of-plane bend (S)	976	976
H_{ring} wag (S)	1133	1132
H_{ring} wag (M)	1161	1160
Ring deformation (C-N asymmetric stretch) (S)	1352	1351
H_{ring} symmetric in-of-plane bend (W)	1440	1437
C=C stretch (W)	1576	1576
H_{ring} symmetric stretch (M)	3125	3125
H_{ring} symmetric stretch (M)	3144	3144

Table S8. Band assignment of IR spectrum of benzene in bulk liquid and in X-ZIF-8.

		$\tilde{\nu}_{Obs.}$/cm^{-1}			
Mode [a,b]	Band	Bulk (liquid)	ZIF-8	Cl-ZIF-8	Br-ZIF-8
ν_{11}	C-H bend	673	672	670	672
ν_{18}	C-C stretch	1035	1034	1026	1034
ν_9	C-H bend	1176	1179	1165	----
ν_{14}	C-C stretch	1309	1309	1312	----
ν_{19}	C-H bend	1479	1478	1478	1478
ν_8	C-C stretch	1586	1579	1577	1576
ν_7	C-H stretch	3035	3034	3034	3033
ν_{20}	C-H stretch	3071	3070	3070	3069
ν_2	C-H stretch	3091	3089	3090	3088

a) Ref. [S3]

b) Ref. [S4]

Table S9. The parameters characterizing the ^{13}C NMR resonance lines in ZIF-8 and ZIF-8/C_6H_6.

	ZIF-8			ZIF-8/C_6H_6		
	δ / ppm	σ / ppm	Intensity	δ / ppm	σ / ppm	Intensity
Me	13.63	0.35	3.9	14.8	0.3	3.3
Imidazole ring						
C(2)_comp1	150.8	0.6	1.6	150.8	0.48	1.15
C(2)_comp2	151.75	0.45	0.85	151.6	0.45	0.55
C(2)_comp3	153	2.5	0.3	----	----	----
C(4,5)_comp1	123.2	2.5	0.6	----	----	----
C(4,5)_comp2	123.2	0.52	1	124.2	0.49	1
C(4,5)_comp3	124.55	0.62	2.65	125.3	0.55	2.2
Benzene	----	----	----	127.67	0.32	11.3

Table S10. The parameters characterizing the ^{13}C NMR resonance lines in Cl-ZIF-8 and Cl-ZIF-8/C_6H_6.

	Cl-ZIF-8			Cl-ZIF-8/C_6H_6		
	δ / ppm	σ / ppm	Intensity	δ / ppm	σ / ppm	Intensity
C(2)_comp1	135.5	0.45	0.4	136.75	0.7	0.85
C(2)_comp2	136.69	0.43	2.7	137.45	0.65	0.8
C(2)_comp3	138.05	0.46	1.4	138.35	0.8	0.9
C(2)_comp4	139.15	0.75	1.5	----	----	----
C(4,5)_comp1	125	0.5	2.6	125.5	0.75	1.6
C(4,5)_comp2	126.23	0.7	6.45	126.6	0.65	3.5
Benzene	----	----	----	127.6	0.35	28

Table S11. The parameters characterizing the ^{13}C NMR resonance lines in Br-ZIF-8 and Br-ZIF-8/C_6H_6.

	Br-ZIF-8			Br-ZIF-8/C_6H_6		
	δ / ppm	σ / ppm	Intensity	δ / ppm	σ / ppm	Intensity
C(2)_comp1	120.5	4.0	0.5	122	3	0.3
C(2)_comp2	127.2	4.0	0.5	124.7	0.55	0.98
C(2)_comp3	----	----	----	123.63	0.55	0.4
C(4,5)_comp1	126.7	0.6	1.3	127.55	0.9	0.9
C(4,5)_comp2	128	0.8	4.3	128.75	0.8	4.4
Benzene	----	----	----	127.85	0.33	17.5

3. Evaluation of activation entropy of benzene trapped by 6-membered ring aperture

In order to evaluate the activation entropy, at the first approximation, we accounted for the decrease in the degree of freedom when benzene molecule was trapped on the 6-menbered ring aperture from the vapor phase. In this process, benzene molecules lose the degree of freedom of translation and rotational motions. In the 6-menbered ring aperture, the interaction between a benzene molecule and the 2-imidazolate linkers lowers the frequency of the flipping motion of the linker moiety, resulting in the increase in degree of freedom in the vibrational excitation at a constant temperature. The orientational disorder of the linker moiety will also contribute to the entropy due to the configurations. Furthermore, in ZIF-8, the degree of freedom in the methyl rotation contributes to the molar entropy. Taking account of the molecular partition functions on translational, rotational, and vibrational motions, we evaluated the contributions to the molar entropy from these motional modes [S5].

For the three-dimensional translational motion of benzene, molar entropy, S_m^T, is given by the Sackur-Tetrode equation as follows;

$$S_m^T = Rln\frac{kTe^{5/2}}{p\Lambda^3}$$

where $\Lambda = h/(2\pi mkT)^{1/2}$ that is the thermal wavelength, p is the vapor pressure at temperature, T. For bulk benzene, the vapor pressure is evaluated to be 1.579×10^5 Pa at 303 K using the Antoine equation [S6]. This equation provids 160 JK^{-1} mol^{-1} at 303 K as a molar entropy of bulk benzene.

For rotational motion, molar entropy, S_m^R, is calculated from the molecular partition function, q_R, through the following relation:

$S_m^R = R(1 + lnq_R)$.

Assuming a benzene molecule as a symmetric rigid rotor, the molecular partition function of the rotational motion is given by

$$q_R = \frac{1}{\sigma}\left(\frac{kT}{hc}\right)^{3/2}\left(\frac{\pi}{\tilde{A}^2\tilde{C}}\right)^{1/2}$$

where $\tilde{A}$ and $\tilde{C}$ are rotational constants for the molecular rotation around the C_2- and the C_6-symmetry axes, respectively. They are represented by

$$\tilde{A} = \frac{\hbar}{4\pi cI_{\perp}}$$

and

$$\tilde{C} = \frac{\hbar}{4\pi cI_{||}}$$

where $I_{\perp}$ and $I_{||}$ are moment of inertia of benzene molecule around the C_2- and C_6-symmetry axes, respectively. The symmetry number, σ, is 12 for benzene. This equation provids 82.7 JK^{-1} mol^{-1} at 303 K for isotropic rotation of bulk benzene. The contributions of the molar entropy of rotation around the C_6- and C_2-

symmetry axes are represented, respectively, by the following partition functions:

$$q_R^{C_6} = \frac{1}{\sigma}\left(\frac{kT}{hc}\right)^{1/2}\left(\frac{\pi}{\tilde{A}^2}\right)^{1/2}$$

and

$$q_R^{C_2} = \frac{1}{\sigma}\left(\frac{kT}{hc}\right)\left(\frac{\pi}{\tilde{A}^2}\right)^{1/2}.$$

At 303 K, these equations give a molar entropy of 18.9 JK^{-1} mol^{-1} for uniaxial rotation around a C_6-symmetry axis and of 63.8 JK^{-1} mol^{-1} for rotation around two C_2-symmetry axes.

The methyl group can be treated as a symmetric rigid rotor, and the molecular partition function of the uniaxial C_3-symmetry rotational motion is given by

$$q_R = \frac{T}{\sigma\theta_{R,\,CH_3}}$$

where $\theta_{R,\,CH_3}$ is the rotational temperature of a methyl group, and is given by $hc\tilde{B}/k$ using a rotational constant, $\tilde{B}$, for the rotation around a C_3-symmetry axis. The σ value is 3 for the methyl group.

For the vibrational motion, a molar entropy, S_m^V, is calculated using the following relation;

$$S_m^V = R\left\{\frac{\theta_V/T}{e^{\theta_V/T}-1} - ln\left(1-e^{-\theta_V/T}\right)\right\}$$

where θ_V is the characteristic vibrational temperature, and is given by $hc\tilde{\nu}/k$. The frequencies of the linker flipping have been reported to be 0.58 THz in guest-free ZIF-8 [S7] and 0.053 THz in ZIF-8/benzene (6 molecules per pore) [S8]. The contribution of the molar entropy from the torsional vibration of an imidazolate linker is evaluated for these vibrational frequencies as a function of temperature, increasing the entropy by 20 JK^{-1} mol^{-1} for a linker at 303 K.

4. ^{13}C-^{14}N and ^{13}C-$^{79/81}$Br residual dipolar splitting

The ^{13}C-X ($S > 1/2$) residual dipolar splitting depends on the resonance frequency of X nuclei, Z_S, the X quadrupole coupling constant, $\chi(= e^2q_{zz}Q/h)$, the ^{13}C-X dipolar interaction, D, and the orientation of the ^{13}C-X vector with respect to the EFG principal axis of X nuclei, which is defined by a pair of azimuth α and elevation angle β [S9-S12]. The resonance frequency, ν_m, is shifted by the ^{13}C-X residual dipolar interaction and is given by

$$\nu_m = \frac{3\chi D\left[S(S+1)-3m^2\right]}{20Z_S\quad[S(2S-1)]}f(\alpha,\beta)$$

where $f(\alpha,\beta) = 3\cos^2\beta - 1 + \eta\sin^2\beta\cos 2\alpha$. The value of $f(\alpha,\beta)$ is distributed from -1 to 2 when the asymmetric parameter of the electric field gradient tensor is zero (η = 0). The heteronuclear dipolar interaction, D, is represented by

$$D = \left(\frac{\mu_0}{4\pi}\right)\frac{\gamma_I \gamma_S h}{4\pi^2 r_{IS}^3}$$

for a *I*-*S* nuclear spin pair with the internuclear distance of r_{IS}. The ^{13}C-X residual dipolar splitting, Δ, of the resonance peak is given by $\nu_m - \nu_{m'}$. For ^{13}C-^{14}N pair, $S = 1$ and $\Delta = \nu_0 - \nu_{\pm 1}$. For ^{13}C-$^{79/81}$Br pair, $S = 3/2$ and $\Delta = \nu_{\pm 1/2} - \nu_{\pm 3/2}$.

The typical values of the ^{14}N quadrupole coupling constant for imidazole coordinating to zinc are distributed from 1.9 to 2.8 MHz for imino nitrogen and from 1.5 to 1.8 MHz for amino nitrogen [S13]. Using $\chi \sim 2.8$ MHz and r_{CN} =1.377 Å, the maximum splitting caused by the ^{13}C-^{14}N residual dipolar interaction is estimated to be < 0.2 ppm under the external magnetic field of 14.7 T, which is smaller than the full width at a half maximum of the observed peak (the σ values in Table S8 are distributed in the range from 0.45 ppm to 2.5 ppm for ZIF-8 and ZIF-8/C_6H_6).

On the other hand, in the case of ^{13}C-$^{79/81}$Br, we referred to *p*-dibromoteterafluorobenzene ($C_6F_4Br_2$) for the typical compound with the covalent bond between aromatic carbon and bromine atoms. In this compound, the $^{79/81}$Br quadrupole coupling constants are ~ 515 MHz for ^{81}Br nuclei and ~ 617 MHz for ^{79}Br nuclei [S14]. These values are regarded as the typical values of the $^{79/81}$Br quadrupole coupling constant for bromine atom covalently bonded to the benzyl group. In addition, using r_{CBr} =1.872 Å in Br-ZIF-8, the maximum splitting is estimated at 15ppm for ^{81}Br and at 19 ppm for ^{79}Br under the external magnetic field of 14.7 T. These values are reasonable for the observed linewidth for the quaternary carbon of Br-ZIF-8.

References

[S1] B. Xu, D. Xie, Y. Mei, Z. Kang, R. Wang, D. Sun, *Phys. Chem. Chem. Phys.,* 2017, **19**, 27178-27183.

[S2] C. Wu, D. Xie, Y. Mei, K. M. Poduska, D. Li, B. Xu, D. Sun, *Phys. Chem. Chem. Phys.,* 2019**, 21**, 17571-17577.

[S3] M. A. Palafox, Scaling factors for the prediction of vibrational spectra. I. Benzene molecule. *Inter. J. Quant. Chem*., 2000, **77**, 661-684.

[S4] S. Brodersen, A. Langseth, *Mat. Fys. Skr. Dan. Vid. Selsk*., 1956, **1**, 1.

[S5] P. Atkins, J. de Paula, *Atkins' Physical chemistry, tenth edition*; Oxford University Press: Oxford, U.K., **2014**; pp. 636–643.

[S6] C.B. Willingham, W. J. Taylor, J. M. Pignocco, F. D. Rossini, Vapor pressures and boiling points of some paraffin, alkylcyclopentane, alkylcyclohexane, and alkylbenzene hydrocarbons, *J. Res. Natl. Bur. Stan.*, 1945, **35**, 3, 219-217.

[S7] T. Ueda, M. Nakai, T. Yamatani, A solid-state ^{1}H-NMR study of the dynamic structure of ZIF-8 and its role in the adsorption of bulky molecules, *Adsorption*, 2017, **23**, 887–901.

[S8] D. I. Kolokolov, A. G. Stepanov, H. Jobic, Mobility of the 2-Methylimidazolate Linkers in ZIF-8 Probed by ^{2}H NMR: Saloon Doors for the Guests, *J. Phys. Chem. C*, 2015, **119**, 27512–27520.

[S9] R. K. Harris, A. C. Olivieri, Quadrupolar Effects Transferred to Spin-1/2 Magic-Angle Spinning Spectra of Solids, *Prog Nucl Magn Reson Spectrosc*, 1992, **24**, 435-456.

[S10] A. C. Olivieri, L. Frydman, L. E. Diaz, A Simple Approach for Relating Molecular and Structural Information to the Dipolar Coupling ^{13}C-^{14}N in CPMAS NMR, *J. Magn. Reson.*, 1987, **75**, 50-62.

[S11] A. C. Olivieri, Quadrupolar Effects in the CPMAS NMR Spectra of Spin-1/2 Nuclei, *J. Magn. Reson.*, 1989, **81**, 201-205.

[S12] K. Eichele, M. D. Lumsden, R. E. Wasylishen, Nitrogen-14 Coupled Dipolar-Chemical Shift ^{13}C NMR Spectra of the Amide Fragment of Peptides in the Solid State, *J. Phys. Chem.*, 1993, **97**, 8909-8916.

[S13] C. I. H. Ashby, C. P. Cheng, T. L. Brown, ^{14}N Nuclear Quadrupole Resonance Spectra of Coordinated Imidazole, *J. Am. Chem. Soc.*, 1978, **100**, 6057–6063.

[S14] P. C. Cerreia Vioglio, P. M. J. Szell, M. R. Chierotti, R. Gobetto, D. L. Bryce, $^{79/81}$Br Nuclear Quadrupole Resonance Spectroscopic Characterization of Halogen Bonds in Supramolecular Assemblies, *Chem. Sci.*, 2018, **9**, 4555.